Electronic Supplementary Material (ESI) for Nanoscale.

Electronic Supplementary Information for: Emergent magnetic texture in driven twisted bilayer graphene

Dario A. Bahamon,[*a] G. Gómez-Santos,[b] and T. Stauber[c]

Coherent transport properties of twisted bilayer graphene

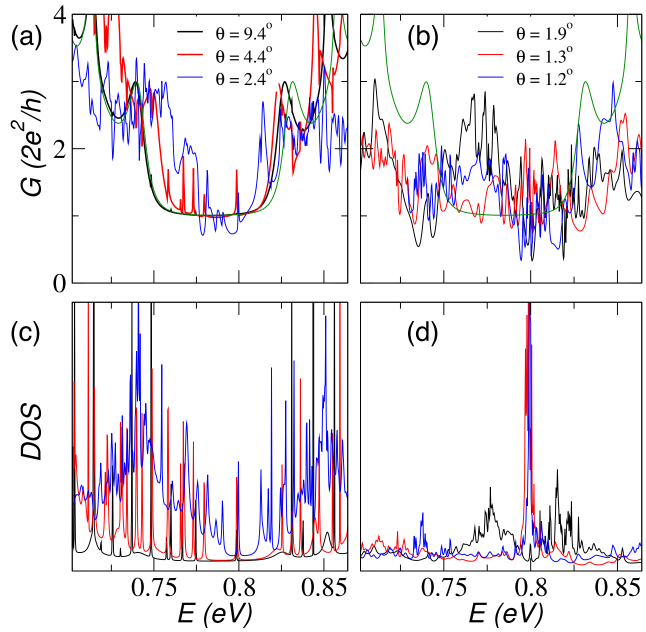

Fig. S1 Conductance of the twisted bilayer graphene barrier in the (a) intermediate twist angle regime for $\theta = 9.4°(i = 3)$, $4.4°(i = 7)$ and $2.4°(i = 13)$. (b) Small twist angle regime for $\theta = 1.9°(i = 17)$, $1.3°(i = 24)$ and $1.2°(i = 27)$. The green line on both panels (a-b) corresponds to the conductance of monolayer armchair graphene nanoribbon. (c) Density of States (DOS) for twist angles presented in panel (a). (d) DOS for twist angles in panel (b).

Conductance, momentum mismatch and charge neutrality point

This section contains a detailed discussion of the conductance and Density of States (DOS) observed in the twisted bilayer graphene (TBG) barrier. In Fig. S1 (a), the conductance for the TBG barrier is shown for intermediate twist angles. The strength of the TBG barrier for $\theta = 9.4°(i = 3)$ is still very weak and the conductance lineshape is similar to the conductance for twist angles $\theta > 10°$ (green line in Fig. S1a). For $\theta = 4.4°(i = 7)$, there are resonant peaks superimposed on the first conductance plateau. There is also a reduction on the width of the same plateau. For $\theta = 2.4°(i = 13)$ the first conductance plateau is strongly reduced.

Irrespective of the rotation angle, there are two key attributes in the conductance of the TBG barrier in this twist angle regime: (i) the reduction of the twist angle introduces a continuous set of conducting states, since there are energy regions with conductance values higher than the ones obtained for the weak coupling regime. In those regions, interference is seen which is a consequence of having more than one conducting channel.[1] (ii) There is a conductance peak at $E \sim 0.8$ eV.

The physical origin of both attributes can be deduced from the DOS, shown in Fig. S1 (c). The first conductance feature can be

[a] MackGraphe – Graphene and Nano-Materials Research Center, Mackenzie Presbyterian University, Rua da Consolação 896, 01302-907, São Paulo, SP, Brazil; E-mail: dario.bahamon@mackenzie.br
[b] Departamento de Física de la Materia Condensada, Instituto Nicolás Cabrera and Condensed Matter Physics Center (IFIMAC), Universidad Autónoma de Madrid, E-28049 Madrid, Spain
[c] Departamento de Teoría y Simulación de Materiales, Instituto de Ciencias de Materiales de Madrid, CSIC, E-28049, Madrid, Spain;E-mail: tobias.stauber@csic.es

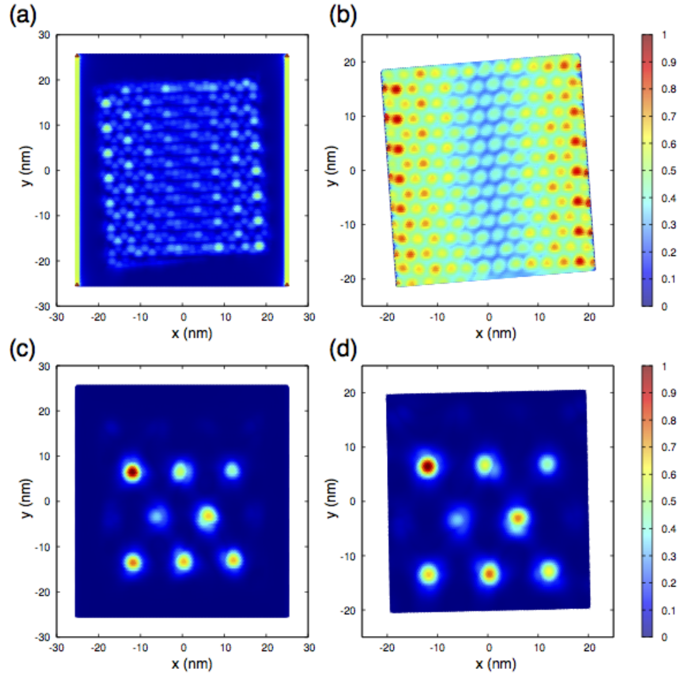

Fig. S2 Local Density of States for $\theta = 4.4°(i = 7)$ and $E = 0.8$ eV: (a) bottom layer; (b) top layer. Local Density of States for $\theta = 1.2°(i = 27)$ and $E_F = 0.8$ eV: (c) bottom layer; (d) top layer.

understood by noticing that new conducting states rise around $E \sim 0.8$ eV when the twist angle is reduced. On the other hand, the transmission peak at $E \sim 0.8$ eV signals the position of the charge neutrality point (CNP) of the TBG barrier. This can be understood by noticing that the highly doped left contact injects electrons with a defined momentum k_c which are scattered into a number of available states with momentum $k_x^{\mathrm{TBGb}} = V_g/\hbar v_F$, where $V_g = E_F - E_{\mathrm{CNP}}$ is the gate voltage[2] and E_{CNP} the energy at the CNP. At the CNP, the mismatch between the available momenta in the contacts (k_c) and the TBG barrier ($k_x^{\mathrm{TBG}} = 0$) produces an evanescent state and partial reflection at the barrier. The constructive interference between these waves produces a transmission peak.[3]

Notice that the momentum mismatch and E_{CNP} hardly depend on the twist angle and the peaks in the conductance and DOS observed for all twist angles at $E \sim 0.8$ eV indicate the position of E_{CNP}. The appearance of the high DOS peak at the same energy in the small angle regime confirms that our transport analysis is correct.

In the small angle regime ($0° < \theta < 2°$), the conductance quantization is completely gone. We can see in Fig. S1 (b) that the conductance shows rapid oscillations around $E \sim 0.8$eV and the frequency as well as the intensity of these oscillations increase as the angle is reduced. The TBG barrier thus again scatters incident electrons into different channels with the same energy. However, in the small angle regime there is a higher DOS around $E \sim 0.8$eV, shown in Fig. S1 (d). Consequently, the electrons transmit through a larger number of propagating states generating more complex interference patterns.

Local Density of States

In Fig. S2 (a) and (b), we have plotted the local Density of States (LDOS) for the for the state at $E = 0.8$eV and twist angle $\theta = 4.4°$. The state presents all the characteristics of an evanescent state: high LDOS at the edges that decays towards the center of the TBG barrier. However, the top and bottom layer are still weakly coupled since the LDOS is not evenly distributed over both layers. Consequently, in this regime the top patch behaves as an additional channel for the transport.

In the small angle regime, the interference discussed above is also appreciated looking at LDOS. In Fig. S2 (c) and (d), the LDOS is shown for $\theta = 1.2°$ at $E = 0.8$eV. The high LDOS is unevenly distributed over the AA-stacked regions as a result of the multiple electronic paths. The lower LDOS in the regions close to the edges of the top graphene flake are finite size effects indicating a reduction of the Moiré confinement potential. In the small angle regime, electrons thus transmit through the sample via a number of degenerate states localized on AA-stacked regions.

Charge neutrality of bulk TBG

For an additional confirmation of the CNP location, we calculated the band structure for bulk TBG for different twist angles. The CNP of the bulk system is located around the same value we obtained from transport calculations of our finite system, see Fig. S3.

Based on the above and the conductance calculation, we can confirm that our finite system reproduces the main features reported for bulk TBG for $\theta > 1^\circ$. Although DOS plots of our device show oscillations due to the confinement, we clearly observe: (i) new vHs with the reduction of the twist angle, (ii) Merging of vHs for small angles and (iii) localization of the wave function on AA-stacked regions.

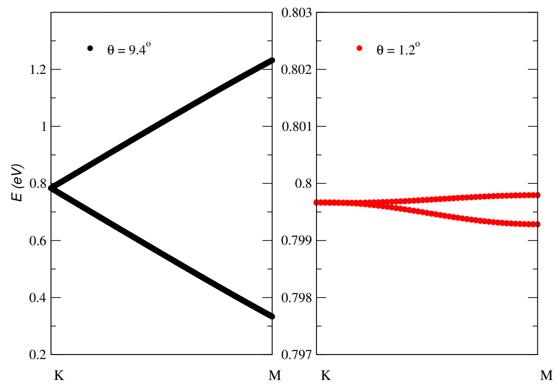

Fig. S3 Band structure around the charge neutrality point for bulk twisted bilayer graphene for twist angles $\theta = 9.4^\circ$ and $\theta = 1.2^\circ$).

Twist angles beyond the magic angle

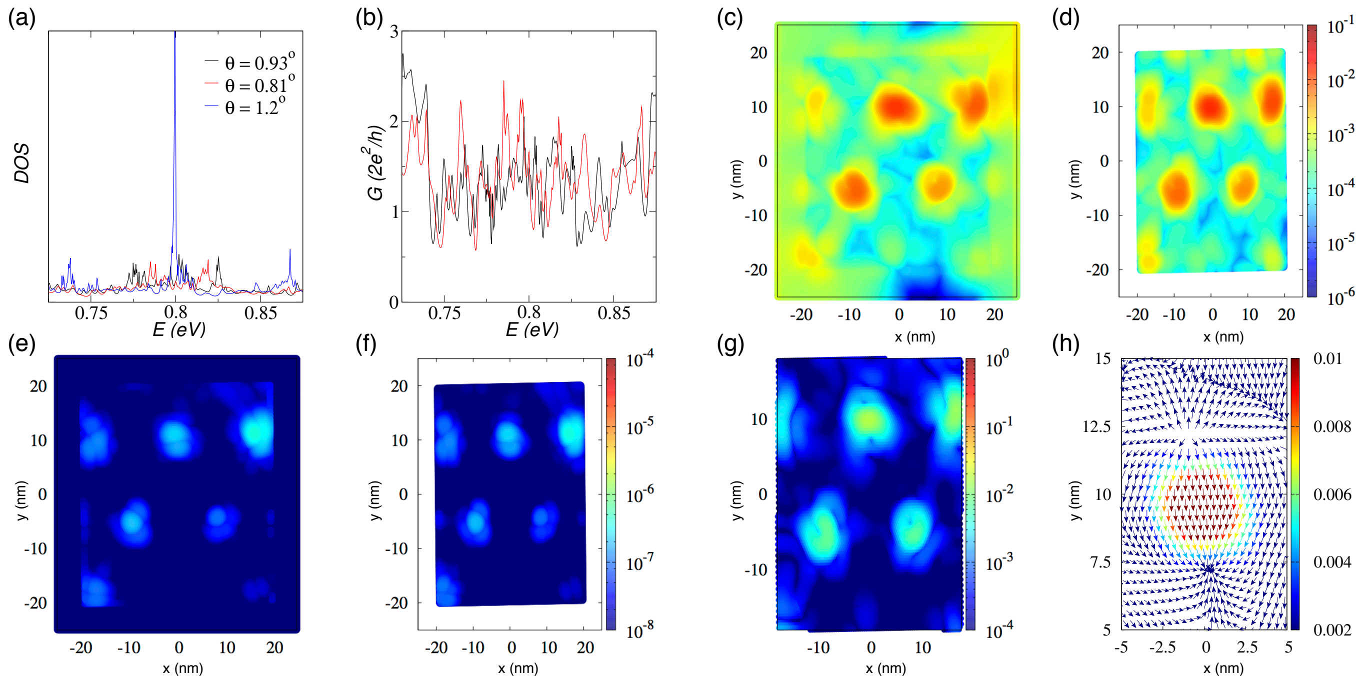

Fig. S4 DOS (a) and conductance (b) for twist angles $\theta = 0.93^\circ (i = 35)$ and $\theta = 0.81^\circ (i = 40)$. The blue line in panel (a) corresponds to the DOS for $\theta = 1.2^\circ$. Total current normalized by the total source-drain current per bond for bottom (c) and top (d) layer. (e)-(f) In-plane magnetic moment calculated by $\vec{m} = \sum_{<ij>} I_{ij}(\vec{r}_i \times \vec{r}_j)/2$ in units of Bohr magneton for bottom and top layers. (g) Magnitude of the counterflow current ($|\vec{I}_m|$) normalized by the total source-drain current per bond. (h) Vectorial map of $\vec{I}_m$ over one AA-stacked region. In panels (c)-(h), the parameters are: $\theta = 0.81^\circ (i = 40)$, $V_g = 0.1$ meV and $V_{SD} = 100\ \mu$V.

For $\theta < 1^\circ$, there is no high DOS at the charge neutrality point as shown in Fig. S4 (a). Still, there is a high LDOS on the AA-stacked regions. For small twist angles, the Moiré periodicity $D = a/\sin(\theta/2) > 16.2$ nm almost exceeds the dimension of the top layer and the few AA-stacked regions are not enough to produce a DOS peak at the CNP. From the transport point of view, the TBG efficiently scatters electrons into the available states producing interference as seen from the rapid oscillations in the conductance, see Fig. S4 (b).

Regarding the main results presented in the main text, we continue observing high current density and in-plane magnetic moments on the AA-stacked regions since these effects are the result of having high LDOS on those regions. To assert the above mentioned, we plot for a TBG barrier with $\theta = 0.81^\circ (i = 40)$, $V_g = 0.1$ meV and $V_{SD} = 100\ \mu$V the magnitude of the electric current divided by the source-drain current per bond in Fig. S4(c)-(d) and the in-plane magnetic moment in panels (e)-(f) calculated by the global formula $\vec{m} = \sum_{<ij>} I_{ij}(\vec{r}_i \times \vec{r}_j)/2$. The maps allow us to identify that in spite of the low number of AA-stacked regions the injected current still produces charge current and in-plane magnetic moments “hot spots”. Moreover, because of the greater Moiré periodicity the in-plane magnetic moments appear totally localized on the central AA-stacked regions. The current counterflow maps (Fig. S4(g)-(h)) also show high values and preferred orientation on the same regions.

Local definition of the magnetic moment and chiral response

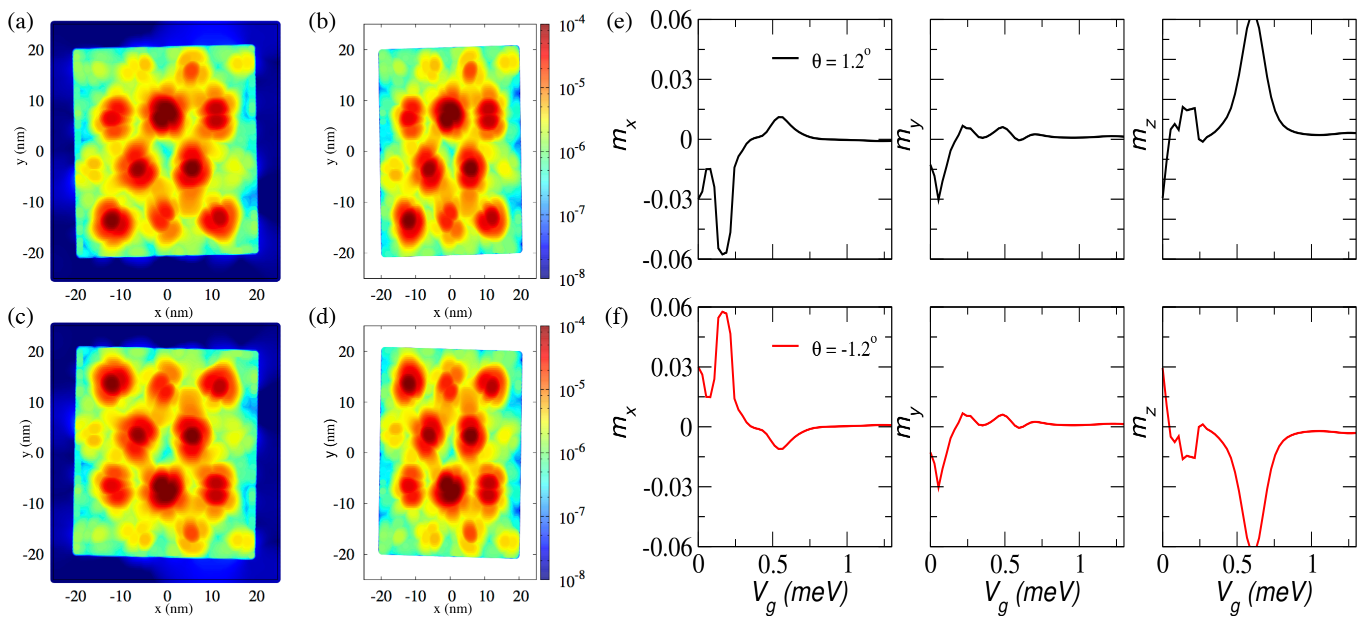

Fig. S5 Map of the in-plane magnetic moment for $\theta = 1.2^\circ$, see panels (a) and (b), and $\theta = -1.2^\circ$, see panels (c) and (d), at gate voltage $V_g = 0.1$ meV. Components of the magnetic moment as function of V_g for $\theta = 1.2^\circ$, see panel (e), and $\theta = -1.2^\circ$, see panel (f). In all panels, the magnetic moments are in units of μ_B and $V_{SD} = 100\ \mu$V

To check if the system size allows for a general analysis, we perform the calculations for a positive and negative twist angle. The infinite twisted bilayer system can be transformed from a positive to a negative twist angle by performing a parity-transformation $\vec{r} \to -\vec{r}$ and subsequent mirror-transformation (π rotation around the y-axis). The position vector, current density, and magnetic moment transform accordingly, i.e., $(x,y,z) \to (x,-y,z)$, $(j_x, j_y, j_z) \to (j_x, -j_y, j_z)$, and $(m_x, m_y, m_z) \to (-m_x, m_y, -m_z)$.

In Fig. S5, we can see that our finite system fullfil these requirements. Looking first at the map of in-plane magnetic moment ($V_g = 0.135$ meV and $\theta = \pm 1.2^\circ$) in panels (a)-(d), a large magnetic moment is seen at the AA-stacked regions. These regions transforms as $(x,y,z) \to (x,-y,z)$ and can be linked to the high LDOS and current densities , present on the same spots. To underline the transformation of the magnetic moment, we plot the components $m_{x(y)(z)}$ in units of μ_B as function os V_g in panels (e)-(f). Let us also mention that the sign change of m_x under the transformation points at the chiral coupling of TBG as discussed in Ref. 4.

Defining the in-plane magnetic moment

The calculation of the magnetic and total current at the atomic sites is only well-defined in the AA-stacked regions where the atoms have approximately the same x and y coordinates. At these sites, $\vec{I}_m(x,y) = [\vec{I}_1(x,y) - \vec{I}_2(x,y)]/2$ and $\vec{I}_T(x,y) = \vec{I}_1(x,y) + \vec{I}_2(x,y)$ are well defined. To extend the calculation to other regions of the device, it is necessary to average the current on both layers. Our process is divided in two steps.

- The current on the top layer is averaged at the center of each hexagonal plaquette. To avoid double counting of the atomic sites, we average over the centers of every third hexagonal plaquette which form a triangular lattice with lattice parameter $3a$, where a is the carbon-carbon distance. To cover up the top layer, we have three different possible triangular lattices. These are identified in Fig. S6 (a) by the symbols $\square$, $\diamond$ and $\triangle$. We used these lattices to define the current for each in the hexagonal plaquettes of the top layer as:

$$\vec{I}_2^{\square(\diamond)(\triangle)} = \sum_{s=1}^{6} \vec{I}_2(s) \tag{1}$$

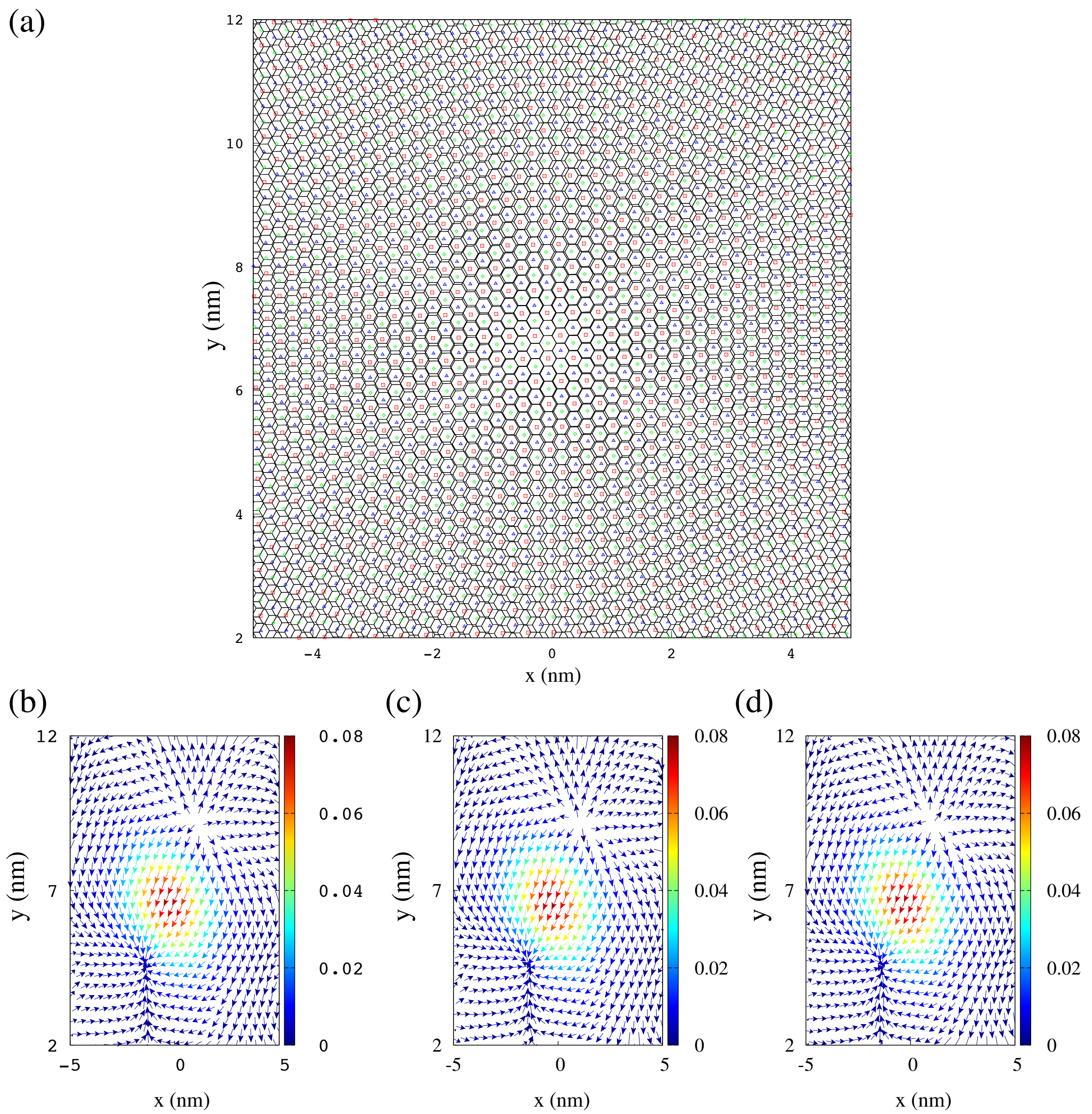

Fig. S6 (a) Real atomic lattice and the dual triangular lattices □, ⋄ and △ used to average the magnetic and total current. Vector map of $\vec{I}_m$ normalised by the total source-drain current per bond for triangular lattice (b) □, (c) ⋄ and (d) △. In panel (b) to (d) $\theta = 1.2°$, $V_g = 0.1$ meV and $V_{SD} = 100\ \mu$V

- The current in the bottom layer, $\vec{I}_1$, is averaged using the same triangular lattice defined for the top layer, but this time we select the atomic sites within a radius $R = 1.5a$:

$$\vec{I}_1^{\square(\diamond)(\triangle)} = \sum_{<1.5a} \vec{I}_1 \,. \tag{2}$$

Using the above procedure the coordinates of the top and bottom current are the same and we can proceed to calculate $\vec{I}_m$ and $\vec{I}_T$.

To confirm that the results obtained do not (strongly) depend on triangular lattice used, we present the resulting magnetic current using the local definition in Fig. S6 (b) - (d). It is clearly appreciated that the enhanced counterflow current in AA-stacked regions remains a robust feature irrespective of details of the calculation method.

Perturbations

Lattice relaxation

Let us analyze in more detail the effect of lattice relaxation following the approach by Nam and Koshino.[5,6] We first present the source to drain current for the relaxed lattice that we used to normalise the current maps in the main text. In Fig. S7 (a), we show the calculated current as function of the gate voltage for $\theta = 1.2°$, $V_{SD} = 100\ \mu$eV.

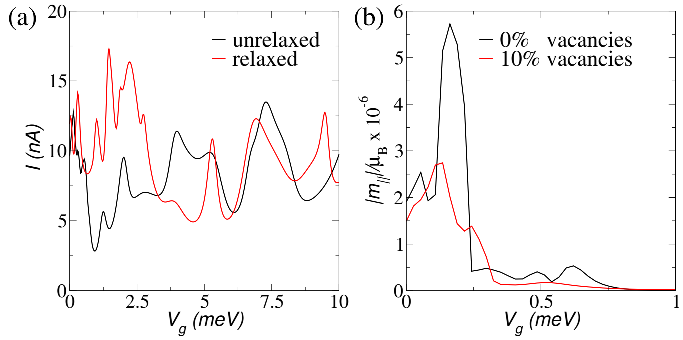

Fig. S7 (a) Source-drain current for the (un)relaxed device. The relaxation parameters were taken from Nam and Koshino.[5,6] (b) In-plane magnetic moment per site as function of the gate voltage around the AA-stacked region between $-5 \leq x/\text{nm} \leq 5$ and $2 \leq y/\text{nm} \leq 12$ calculated via the global formula of the magnetic moment. The values were obtained by averaging over 5 randomly distributed vacancy realizations. In all panels, we considered $\theta = 1.2^\circ$ and $V_{SD} = 100\ \mu$eV.

Vacancies

Vacancies in graphene induce the formation of localised states that can perturb the current distribution.[?] In our device with armchair edges, we observe a reduction in the value of the in-plane magnetic moment for the region between $-5 \leq x/\text{nm} \leq 5$ and $2 \leq y/\text{nm} \leq 12$. This is shown in Fig. S7 (b) for a density of 10% of vacancies in the top flake edges having considered 5 randomly distributed vacancy realizations. We observe that the overall in-plane magnetic moment is robust against vacancies

Zigzag edges

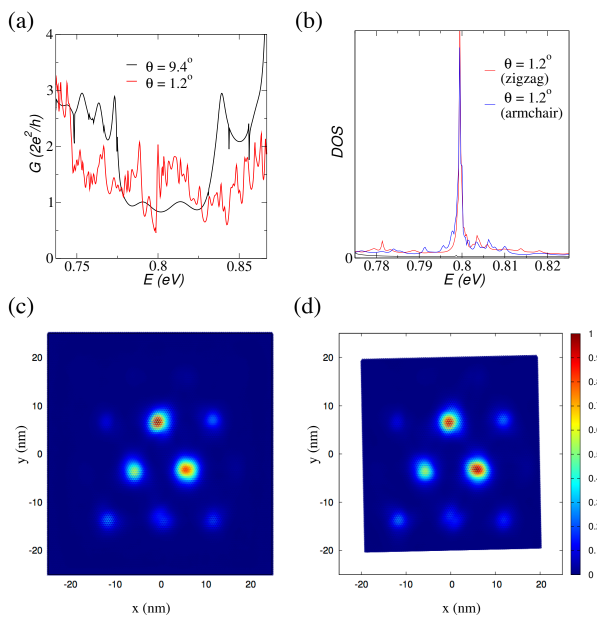

Fig. S8 For the TBG barrier with the zigzag graphene nanoribbon as the bottom layer. (a) Conductance. (b) DOS. The lower panels show the local Density of States for $\theta = 1.2^\circ (i = 27)$ and $E_F = 0.8$ eV: (c) bottom layer; (d) top layer.

We finally present the results for the TBG barrier embedded on top of a zigzag nanoribbon. For large angles, both layers are decoupled and the conductance is the same as the conductance of the single monolayer with zigzag edges. However, compared with armchair case the Fabry-Perot oscillation are more pronounced, see Fig. S8 (a). Similar to the armchair case, we observe a high DOS at the CNP. Also, the local DOS at this energy shows wavefunction localisation on the AA-stacked regions.

Spatial Distribution of Currents in Twisted Bilayer Graphene in the Continuum Model

Here we discuss the spatial distribution of currents induced by the adiabatic introduction of a uniform vector potential along the negative x axis acting only on the layer 2, within the continuum model of Lopes dos Santos et al.[7] The transient electric field points towards the positive x axis and is therefore restricted to the layer 2, but currents are generated in both layers. We expect this asymmetric driving to best mimic the scattering calculation of the main text, even though the geometry differs: here the calculation corresponds to an infinite

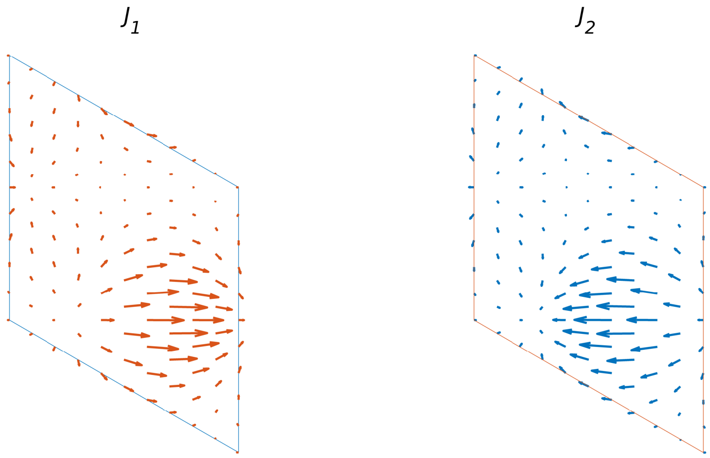

Fig. S9 : Current map (band average) within the Moiré unit cell for twist angle $\theta = 1.05^\circ (i = 31)$, as obtained from the continuum model of Ref.[7]. The current is the response to the adiabatic introduction of a uniform vector potential along the negative x axis acting *only* on the layer 2. The current is strongly enhanced around the AA-stacked region (center of lower triangle) and minimal around the AB-stacked (corners) and BA-stacked (center of upper triangle) regions. Notice that the current of layer 2 is opposite to the field direction giving rise to a paramagnetic response.

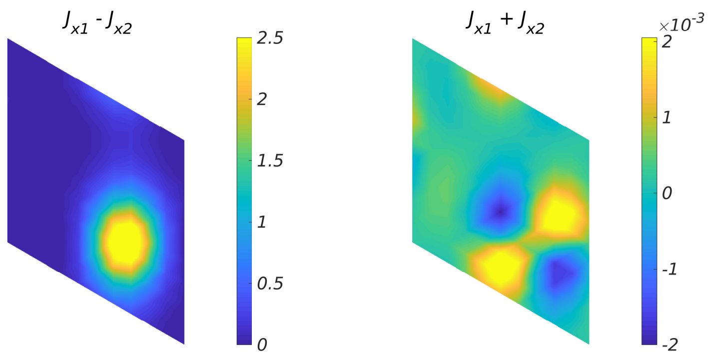

Fig. S10 : Left panel: Counterflow current map (band average) within the Moiré unit cell. Right panel: Total current map (band average) within the Moiré unit cell. Units are arbitrary but the same for both panels and notice the huge difference in scales between both cases.

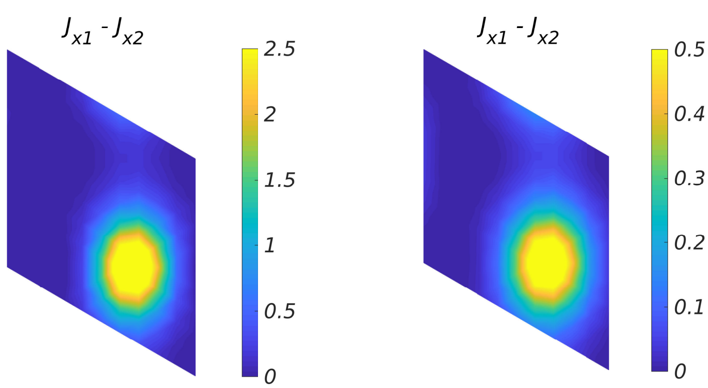

Fig. S11 : Left panel: Counterflow current (band average) for the unrelaxed lattice within the Moiré unit cell. Right Panel: As in the left panel for the lattice with relaxation.

system. The twist angle is $\theta = 1.05^\circ (i = 31)$ and the intra and interlayer hopping parameters are given by $t = 3$eV and $t_\perp = 0.12$eV (the value quoted for $t_\perp$ in the SI of Ref.[4] should be divided by 3). The calculation is standard linear response for the continuum model[4], adapted to obtain the response current at position $\boldsymbol{r}$, given by

$$\boldsymbol{j}(\boldsymbol{r}) = \frac{ev_F}{2}(|\boldsymbol{r}\rangle\langle\boldsymbol{r}|\boldsymbol{\sigma} + \boldsymbol{\sigma}|\boldsymbol{r}\rangle\langle\boldsymbol{r}|), \tag{3}$$

where $\boldsymbol{\sigma}$ are pseudospin (current) operators. The calculation is restricted to Fermi levels within the lowest electron and hole bands around the neutrality point. Main results are:

1) The current is largest in the AA-stacked region, and opposite in both layers with near cancellation, as expected from previous work[4,8]. This is a generic property of the considered bands, as shown in Fig. S9, where the currents averaged for Fermi levels spanning the lowest electron and hole bands is presented.

2) The near cancellation makes the counterflow (*magnetic*) current, $\boldsymbol{J}_1 - \boldsymbol{J}_2$, to be largely enhanced in the AA-stacked regions as compared to the total current, $\boldsymbol{J}_1 + \boldsymbol{J}_2$. This is shown in Fig. S10 where the counterflow current exceeds the total current by three orders of magnitude. In fact, this is a conservative estimate because Fig. S10 represents the band average whereas the enhancement factor can be nominally infinite at the Dirac point, where the total current should vanish but the counterfow does not[4,8].

3) We have also mimicked the presence of lattice relaxation by a 20-percent weakening of the AA interlayer hopping as compared to the AB one in the continuum model. The previous conclusions are hardly affected by this change, as shown in Fig. S11 where the counterflow currents are represented for both the undistorted and distorted cases.

All these features agree with the main message of this work: enhanced counterflow in AA-stacked regions close to the magic angle. It is interesting to remark that, although the total current flows in the positive x-direction, which coincides with the (transient) electric field as expected, the current in the layer where the field is applied (layer 2) runs opposite to the field, see right panel of Fig. S9. This fact is at the heart of the large paramagnetic response previously reported.[4,8]

References

1 J. W. González, H. Santos, E. Prada, L. Brey and L. Chico, *Phys. Rev. B*, 2011, **83**, 205402.

2 J. Tworzydło, B. Trauzettel, M. Titov, A. Rycerz and C. W. J. Beenakker, *Phys. Rev. Lett.*, 2006, **96**, 246802.

3 L. Chico and W. Jaskólski, *Phys. Rev. B*, 2004, **69**, 085406.

4 T. Stauber, T. Low and G. Gómez-Santos, *Phys. Rev. Lett.*, 2018, **120**, 046801.

5 N. N. T. Nam and M. Koshino, *Phys. Rev. B*, 2017, **96**, 075311.

6 N. N. T. Nam and M. Koshino, *Phys. Rev. B*, 2020, **101**, 099901.

7 J. M. B. Lopes dos Santos, N. M. R. Peres and A. H. Castro Neto, *Phys. Rev. Lett.*, 2007, **99**, 256802.

8 T. Stauber, T. Low and G. Gómez-Santos, *Phys. Rev. B*, 2018, **98**, 195414.